Journal of
Materials Chemistry A

ROYAL SOCIETY
OF CHEMISTRY

PAPER

View Article Online
View Journal | View Issue

Cite this: *J. Mater. Chem. A*, 2025, **13**, 30382

High-temperature composite phase change material with "concrete-like" strength even beyond the eutectic temperature

Yuto Shimizu, [a] Takahiro Kawaguchi, [b] Joshua Chidiebere Mba, [b] Tomokazu Nakamura, [b] Keita Tanahashi, [b] Melbert Jeem [b] and Takahiro Nomura *[b]

Received 19th May 2025
Accepted 7th August 2025

DOI: 10.1039/d5ta03994k

rsc.li/materials-a

The need for medium-to-long-term thermal energy storage has increased in tandem with the widespread adoption of variable renewable energy sources. Latent heat storage using metallic phase change materials (PCMs) presents a promising solution by combining high thermal conductivity with high heat storage density. Recent advances in microencapsulated PCMs (MEPCMs) have addressed corrosion and leakage issues commonly associated with metallic PCMs. This study develops an MEPCM composite using an Al–Cu–Si-based MEPCM as the primary component. This system exhibits a suitable structure, performance, and strength for achieving GW h-scale thermal energy storage systems. The MEPCM composite is fabricated by microencapsulating Al–Cu–Si eutectic alloy powder, which has a eutectic temperature of 520 °C, with an Al oxide shell formed *via* chemical conversion and heat-oxidation treatments, followed by mixing with an alumina sintering aid, forming, and sintering. The composite exhibits a heat storage density of approximately 1.0 GJ m^{-3} under a temperature difference (ΔT) of 200 °C, which is 2–3 times higher than that of conventional sensible heat storage materials. It retains both its heat storage performance and structural integrity after 1000 thermal cycles. The thermal conductivity ranges from 4.1 to 6.6 W m^{-1} K^{-1} between 300 and 600 °C. This study is the first to evaluate the compressive strength of composite PCMs in the liquid state, where the composite retains a compressive strength of 32 MPa at 600 °C, which is comparable to that of ordinary concrete. In the solid state, the composite exhibits 83 MPa at room temperature and 49 MPa at 500 °C. Therefore, MEPCM composites are expected to possess substantial compressive strength for applications in medium-to-high-temperature heat storage and thermal management systems, even beyond the eutectic temperature of the PCM.

1. Introduction

With the large-scale deployment of variable renewable energy aiming to achieve a decarbonized society, advancements in thermal energy storage (TES) and thermal management technologies have become increasingly crucial. The variability of renewable energy has been extensively explored, and strategies using power-to-X systems to convert and store renewable energy, including chemical or thermal energy, are essential.[1] Recently, power-to-heat-to-power energy storage systems, also known as Carnot batteries, have been proposed. Carnot batteries excel over other energy storage technologies in terms of economic viability and geographical constraints.[2–4] In addition, power-to-X-related processes, including the Sabatier reaction,[5–11] Fischer–Tropsch synthesis,[12–14] solid oxide fuel cells, and reversible solid oxide cells,[15–17] have demonstrated that thermal management technologies can enhance device and plant performances, extend their service life, and reduce waste heat. Accordingly, the advancement of heat storage and management technologies is indispensable not only for strengthening sector coupling among the electricity, industry, and transportation sectors,[18–20] but also for improving the efficiency of each process.

In TES systems, three main heat storage technologies are widely recognized: sensible heat storage (SHS), latent heat storage (LHS), and thermochemical heat storage (THS).[21–23] SHS is based on the principle of specific heat capacity, storing heat by raising the temperature of solid or liquid materials. Owing to its ease of handling, SHS is the most widely adopted technology; however, its heat storage density is lower than those of LHS and THS. By contrast, LHS uses the latent heat of solid–liquid phase transitions in phase change materials (PCMs) and offers several advantages, including a high heat-storage density, the ability to supply heat at a constant phase change temperature, operation

---

[a] *Graduate School of Engineering, Hokkaido University, Kita 13 Nishi 8, Kita-ku, Sapporo, 060-8628, Japan*

[b] *Faculty of Engineering, Hokkaido University, Kita 13 Nishi 8, Kita-ku, Sapporo, 060-8628, Japan. E-mail: nms-tropy@eng.hokudai.ac.jp; Tel: +81 11 706 6849. Fax: +81 11 706 6842*

using heat alone, and excellent reusability.[21,24–26] THS systems utilize heat released by reversible thermochemical reactions. Although THS demonstrates excellent heat storage performance, it faces more challenges than SHS and LHS, including a shorter material lifetime, lower heat transfer efficiency, and more complex system design due to the involvement of chemical reactions.[21,23,27] Among these technologies, LHS may be used to achieve a simple TES system due to its inherent characteristics and is also suitable for thermal regulation in processes with temperature fluctuations, such as industrial waste heat and heat from chemical reactions.[28,29] Thermal management using PCMs has been studied and commercialized for low-temperature applications, such as electronic devices[30–33] and Li-ion batteries.[34–40] In the high-temperature range, its application to the thermal regulation of chemical reactions has been demonstrated at the laboratory scale.[9–11,41,42]

PCMs face several practical challenges including leakage during melting, chemical reactivity, and phase separation.[43] The microencapsulation of PCMs is an effective solution to these issues.[28,44–46] The development of microencapsulated PCMs (MEPCMs) has been explored for both organic systems,[44,47–50] which operate at low temperatures, and inorganic salt[51–55] and metal alloy systems,[28,45,46] which operate at medium-to-high temperatures. While organic MEPCMs have attained practical applications,[48–50] the technology for microencapsulated molten salt and alloy-based PCMs remains in its early stages. However, in alloy-based MEPCMs, the development of an Al–Si alloy core with an Al_2O_3 shell[56] has initiated a phase of exponential growth in recent years, resulting in various metallic PCMs with different melting points[46] (such as Ga,[57–59] Sn,[60–65] Sn-alloy,[66,67] Zn–Al,[68–72] Al–Cu–Si,[73] Al–Cu,[74] Al–Si,[56,75–82] Al–Si–Fe,[83] Al–Ni,[84] Al,[85–88] and Cu–Si–Al[89] systems) being encapsulated in ceramic shells. The development of these alloy-based MEPCMs provides a foundation for fabricating LHS materials and thermal management systems applicable in medium-to-high-temperature ranges.

Metal and alloy-based MEPCMs, which function both as LHS materials and ceramic particles, exhibit excellent handling and formability, making them highly promising for use in heat storage and thermal management devices. Composite PCMs have been developed using Al–Si-based MEPCMs,[90–93] which are among the most advanced alloy-based MEPCMs. Furthermore, heat storage and thermal regulation devices have been explored at the laboratory scale,[9–11,41,94,95] with the development of kW h-scale packed-bed LHS systems.[96] Recent reports on the development of Al–Si-based MEPCM composites have demonstrated thermal cycling durability of up to 10 000 cycles.[90] In addition, progress has been made with composites utilizing MEPCMs based on Zn–Al,[70,71] Sn,[97,98] and Sn alloys,[99–101] which continue to evolve as part of broader MEPCM development. Research on thermal management technologies using MEPCMs in temperature-varying processes is advancing. Koide *et al.* proposed using MEPCMs as catalyst supports in CO_2 methanation (the Sabatier reaction), a hydrogen utilization technology, to mitigate catalytic thermal runaway caused by exothermic reactions.[9] Similarly, Cholila *et al.* and Takizawa *et al.* reported the effectiveness of MEPCMs in regulating reaction heat in ammonia decomposition[42] and in chemical-loop reverse water–gas shift reaction processes,[41] respectively. Similar thermal management systems using MEPCMs could be employed in the Sabatier reaction, ammonia thermal decomposition, and reverse water–gas shift reaction, alongside use in various catalytic chemical reactions and temperature-varying processes (such as chemical batteries,[34–40,102] dry reforming,[103,104] and solid oxide fuel cells[15–17]).

In LHS, selecting or developing PCMs with appropriate operating temperatures for specific applications is essential. Furthermore, beyond Al–Si-based and other established systems, developing composite materials comprising alloy-based MEPCMs with various melting points is anticipated to advance future TES and thermal management technologies. Accordingly, this study focuses on eutectic Al–Cu–Si alloy-based MEPCMs with a melting point of 520 °C,[73,105] which could be employed in medium-to-high-temperature thermal utilization technologies. Heat storage technologies operating in this temperature range have been practically implemented in concentrating solar power (CSP) systems using steam Rankine cycles.[106–111] Moreover, both the CSP and TES components of Carnot batteries, which are expected to be developed in the future, could benefit from this technology.[112,113]

To the best of our knowledge, this study is the first to evaluate the mechanical strength of composite PCMs at high temperatures exceeding the melting point of PCMs. While several studies have assessed the compressive strength of composite PCMs based on molten salts,[114–120] Sn-based alloys,[100] and Al[121] systems, all these evaluations have been conducted at room temperature, and none have been performed under high-temperature conditions where the PCM exists in a liquid state. However, in packed-bed TES, thermal stresses induced by the thermal expansion of storage materials pose a risk of structural failure in either the storage medium itself or its container.[122–124] Such cyclic thermal stress resulting from repeated heating and cooling is a well-known concern referred to as thermal ratcheting. Concerning this phenomenon, numerical analyses of thermo-mechanical effects in high-temperature heat storage systems have been conducted based on experimental assessments of material mechanical properties.[125,126] Therefore, to realize the large-scale implementation of TES and thermal management systems using MEPCM composites, experimental evaluation of mechanical strength at high temperatures is essential.

This study evaluates the compressive strength of composite PCMs when the PCM component is in the molten state and discusses the corresponding failure mechanisms. This investigation provides insight into the compressive fracture properties of alloy-based MEPCM composites with the MEPCM as the primary component. In particular, this study aims to develop composite materials with the Al–Cu–Si-based MEPCM as the main component and to evaluate their thermophysical properties, thermal cycling durability, heat storage performance, and thermomechanical properties, along with their compressive strength and compressive fracture mechanisms under high-temperature conditions.

2. Materials and methods

2.1 MEPCM composite preparation

Fig. 1 illustrates the fabrication procedure of the MEPCM composite, which can be broadly categorized into two main steps: (1) MEPCM preparation using Al–Cu–Si alloy particles and (2) MEPCM composite preparation. In step 1, Al–26.5% Cu–5.4% Si (mass%) powder (particle size: $d < 45$ μm) (Hikari Material Industry Co., Ltd., Japan) was used as the raw material. The Al–Cu–Si particles were encapsulated *via* a two-step process comprising a chemical conversion treatment followed by a heat-oxidation treatment (steps 1-1 and 1-2 in Fig. 1). First, 20 g of Al–Cu–Si powder was treated in boiling distilled water containing 16.7 g L^{-1} of Al(OH)$_3$ for 3 h, resulting in the formation of alumina precursors (AlOOH and Al(OH)$_3$) on the particle surface. The treated powder was filtered and dried overnight at 100 °C. In step 1-2, the chemically treated powder underwent heat-oxidation by being heated in ambient air from room temperature to 1100 °C at a rate of 10 °C min^{-1}, followed by isothermal holding for 3 h in a muffle furnace. Fig. 2 presents photographs, scanning electron microscopy (SEM) images, energy dispersive X-ray spectroscopy (EDS) elemental mapping images, and the particle size distribution of the prepared MEPCM samples. The particle size distribution was evaluated using the Segment Anything Model for nanoparticles, as reported by Larsen *et al.*[127] Consistent with a previous study,[73] the MEPCMs were prepared as powders, each comprising an Al alloy core encapsulated by an Al oxide shell (Fig. 2b). In addition, the average particle size of the MEPCM powder was measured as 25.2 μm. In step 2, the MEPCM prepared in step 1 was mixed with a sintering aid powder, shaped into green bodies, and subsequently sintered to form the MEPCM composite (steps 2-1 and 2-2 in Fig. 1). Furthermore, α-Al$_2$O$_3$ (average particle size: 0.15 μm; purity: 99.99%; Taimei Chemicals Co., Ltd., Japan) was used as a sintering aid for the MEPCM composite. The Al–Cu–Si alloy-based MEPCM and the α-Al$_2$O$_3$ powder were wet-mixed at a volume ratio of 8 : 2. The mixed powder was then die-pressed into green bodies with a diameter of 10 mm at 20 MPa for 1 min. The green bodies were sintered by heating in ambient air from room temperature to 1100 °C at a rate of 5 °C min^{-1}, followed by isothermal holding for 1 h in a muffle furnace. After isothermal holding at 1100 °C, the muffle furnace was programmed to cool at a rate of −5 °C min^{-1}. The composite samples were fabricated with weight adjustments to ensure that the height of the green bodies did not exceed approximately 10 mm.

2.2 Analyses

The cross-sectional structure of the MEPCM composite samples was observed and analyzed using SEM and EDS (SEM-EDS; JSM-7001FA, JEOL Ltd., Japan). Fig. S1 provides a schematic of the observed composite region. The sample cross section was prepared by cutting along the central axis of the cylindrical composite, followed by polishing with emery paper. The phase structure of the composite samples was analyzed using powder X-ray diffraction (XRD; MiniFlex600, Rigaku, Japan) with a Cu Kα radiation source. The powder samples for XRD measurements were obtained by grinding the prepared composite samples with a mortar and pestle. The apparent density (ρ_0) of the composite samples at 25 °C was measured using a gas pycnometer (Ultrapycnometer 1000, Quantachrome Instruments, USA). The prepared composite samples were used as-is during the gas pycnometer measurements. The coefficient of linear thermal expansion (α_{CLTE}) of the samples was measured using a thermomechanical analyzer (TMA; TMA7300, Hitachi High-Tech Science Co., Japan). Three composite samples with diameters of 10 mm and heights of approximately 10 mm were prepared and measured using the TMA. The melting and

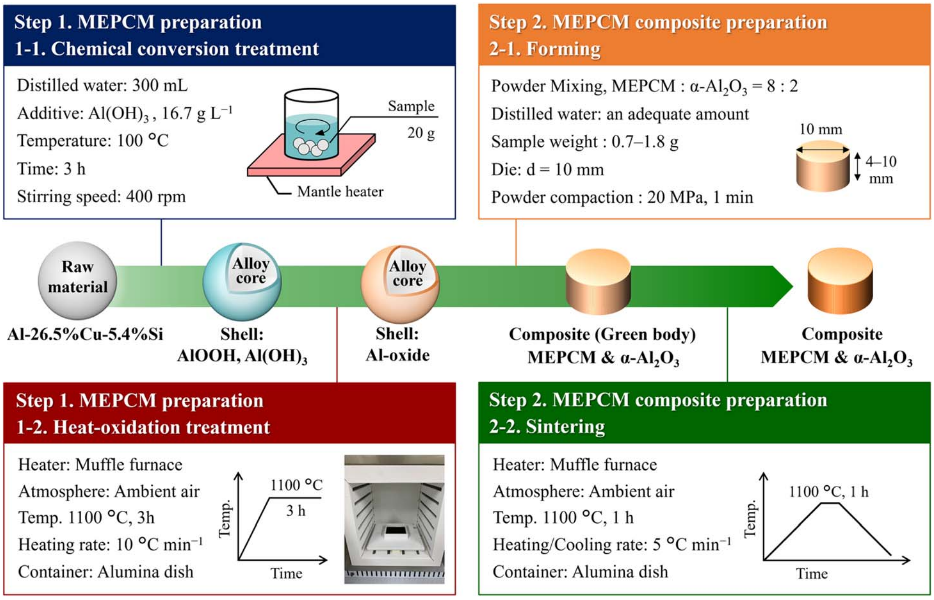

Fig. 1 Preparation procedure of the Al–Cu–Si MEPCM composite.

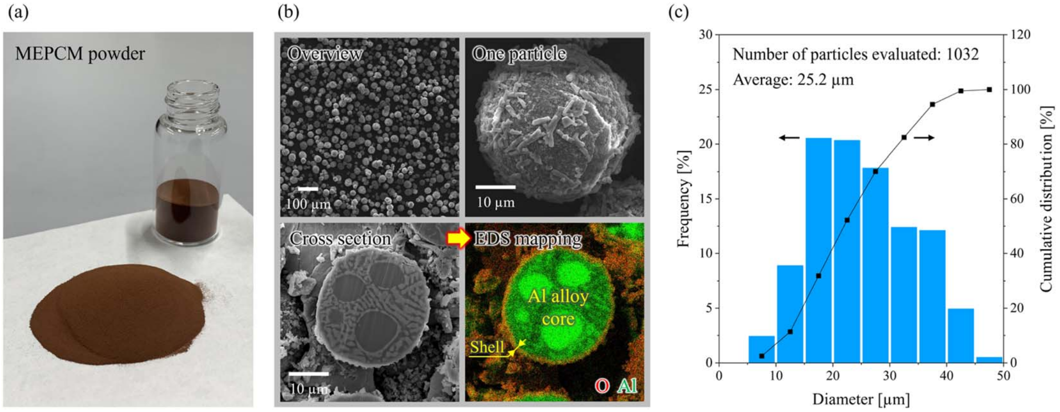

Fig. 2 (a) Photograph of the prepared Al–Cu–Si MEPCM, (b) SEM images of the MEPCM surface, cross section, and EDS elemental mapping of the cross section, (c) particle size distribution of Al–Cu–Si MEPCM.

solidification characteristics of the samples were evaluated using differential scanning calorimetry (DSC; DSC3+, Mettler Toledo, Switzerland). For the DSC measurements, 15 mg of the composite sample, pulverized using a mortar and pestle, was placed in a 30 μL alumina sample pan. The samples were heated to 650 °C under an Ar gas flow of 50 mL min^{-1} and then cooled, with a heating/cooling rate of ±5 °C min^{-1}. The thermal diffusivity (α_{TD}) and specific heat (C_{p}) of the samples were measured using the laser flash analyzer (TC-7000, ULVAC, Japan) over the temperature range of 300–600 °C. For laser flash analysis, samples of the fabricated MEPCM composite were used after thinning to a 1 mm thickness by polishing. The thermal conductivity (k) was calculated using the density (ρ) at a given temperature—determined from the measured ρ_0 and α_{CLTE}—together with α_{TD} and C_{p}. The values of ρ and k were calculated as

$$\rho = \rho_0/(1 + 3\alpha_{\mathrm{CLTE}}(T - T_0)), \tag{1}$$

$$k = \alpha_{\mathrm{TD}} \times C_{\mathrm{p}} \times \rho. \tag{2}$$

2.3 Thermal cyclic test

To evaluate the cyclic durability of heat storage and release, the samples were subjected to 500 and 1000 cycles of heating and cooling within the temperature range corresponding to the melting and solidification of the Al–Cu–Si alloy. For the thermal cycling test, MEPCM composite samples with a diameter and height of 10 and ∼4 mm were used. Fig. 3a shows a photograph of the apparatus used for the thermal cyclic test, while Fig. 3b presents the gas temperature near the sample as measured by thermocouples. The samples were placed in a quartz tube with flowing air and were heated and cooled using two mobile electric furnaces. The temperatures of the two furnaces were set at 400 and 650 °C, respectively. First, the sample was placed at the center of the 400 °C furnace and held until the air temperature in the vicinity of the sample reached a steady state. Then, the 650 °C furnace was moved to the sample position and held there for 6 min, after which the 400 °C furnace was returned to the sample position. Thermal cycling was performed for 500 and 1000 cycles, with heating at 650 °C for 6 min and cooling at 400 °C for 9 min. Based on the gas temperature near the sample during thermal cycling (Fig. 3b), it was confirmed that the sample was heated and cooled within a temperature range of approximately 420–620 °C. The cross-sectional structure and the melting and solidification behaviors of the samples after thermal cycling were analyzed using SEM-EDS and DSC, along with those of the as-prepared MEPCM composite samples.

2.4 Compression test

The composite samples were subjected to compression tests at constant temperatures of 24 (*i.e.*, room temperature (RT)), 500, 550, and 600 °C using a universal testing machine (SHIMADZU

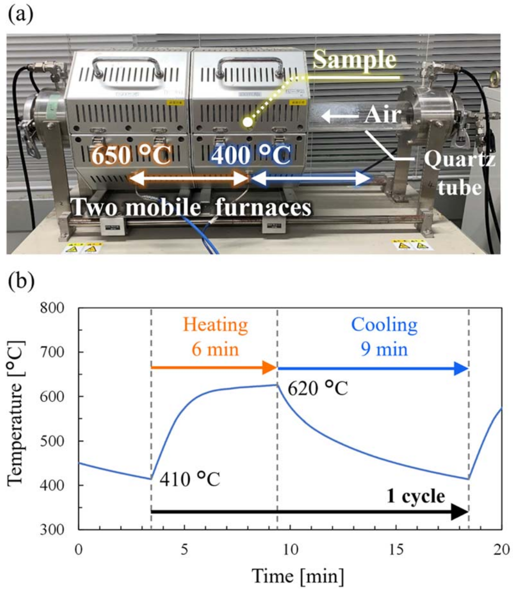

Fig. 3 (a) Photograph of the apparatus used for the thermal cyclic test, and (b) changes in the gas temperature near the sample.

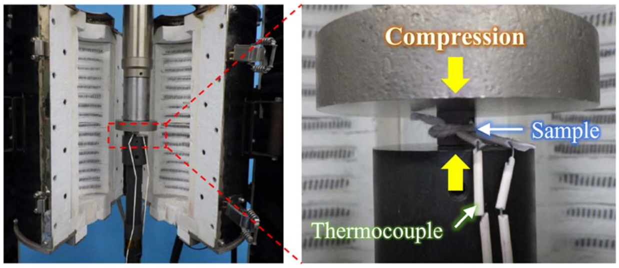

Fig. 4 High-temperature compression test setup.

Co. Ltd., AUTOGRAPH AG-IS 100 kN AG-X/R). The samples attached to thermocouples for temperature control were placed in an electric furnace and compression tested at a compression rate of 0.5 mm min^{-1} in ambient air. Compression tests were performed until the samples were fractured. The setup for the compression tests at an elevated temperature is shown in Fig. 4. Composite samples of 10 mm in diameter and height were used as the compression test specimens. Details of diameter, height, and parallelism for all specimens used in the compression test are listed in Table S1. The cross-sectional sample structure after the compression test was analyzed using SEM-EDS. The as-prepared MEPCM composite samples were also tested.

3. Results

3.1 Structure

Fig. 5 presents multiple characterizations of the Al–Cu–Si-based MEPCM composite: a photograph of the sample (Fig. 5a), SEM and EDS mapping of the cross-sectional structure (Fig. 5b), the XRD pattern (Fig. 5c), and the calculated theoretical density along with the measured apparent and bulk densities (Fig. 5d). As observed in Fig. 5a, no alloy leakage or damage due to cracking occurred even after sintering at 1100 °C. In the sample cross section, microcapsules of Al–Cu–Si alloy covered with Al oxide were sintered to each other while maintaining their respective capsule structures. From the XRD pattern, alloy components Al, Al_2Cu, Si, and Al oxides α-Al_2O_3 and $CuAl_2O_4$ were detected in the composite. Referring to the cross-sectional observation in Fig. 5b, the alloy component comprised the MEPCM core, α-Al_2O_3 comprised the MEPCM shell and sintering aid, and $CuAl_2O_4$ was formed as part of the MEPCM shell. As shown in Fig. 5d, the theoretical density, apparent density, and bulk density of the composite were 3.52, 3.45, and 2.48 g cm^{-3}, respectively. The theoretical density was calculated from the densities of the MEPCM (3.41 g cm^{-3}) and the sintering aid, α-Al_2O_3 (3.96 g cm^{-3}). The mixer volume ratio was 8 : 2. The apparent density was measured using the gas pycnometer, while the bulk density was calculated using the dimensions and weights of the composite samples. These density measurements revealed that the composite sample contained 28.1% and 2.0% open and closed porosities, respectively.

3.2 Phase change properties and thermal cyclic durability

Fig. 6a and b show the DSC curves of the composite during heating and cooling, respectively. An expanded view of the curves in the temperature range of 530–590 °C for the first cycle and after 500 and 1000 thermal cycles is shown in Fig. 6c. The melting onset temperature ($T_{\mathrm{m,onset}}$) of the as-prepared composite (first cycle) was observed at 519 °C, followed by the main melting peak (P_{m1}) at 521 °C. Most of the latent heat of melting was attributed to P_{m1}, although a minor peak (P_{m2}) was observed at 573 °C. The total latent heat capacity of melting (ΔH_{m}) was 190 J g^{-1}. After 500 and 1000 thermal cycles, the values of $T_{\mathrm{m,onset}}$, P_{m1}, and P_{m2} remained unchanged compared to the first cycle. In addition, ΔH_{m} showed negligible variation before and after the thermal cyclic tests. According to the DSC cooling curves in Fig. 6b and c, the solidification onset temperature ($T_{\mathrm{s,onset}}$) of the composite was determined to be 553 °C. However, $T_{\mathrm{s,onset}}$ did not correspond to the main solidification stage, as the primary solidification peaks, P_{s1} and P_{s2}, were observed at 496 and 489 °C, respectively, at lower temperatures. The total latent heat capacity of solidification (ΔH_{s}) was 189 J g^{-1}, which was similar to the latent heat capacity of melting. Similar to the melting behavior, there was almost no change in the $T_{\mathrm{s,onset}}$, P_{s1}, P_{s2}, and ΔH_{s} values before and after the thermal cyclic tests. A discussion of the heat storage properties and thermal cyclic durability of this system based on the results of this cycle test is provided in Section 4.1.

Fig. 7a-1–a-3 present SEM images and Fig. 7b-1–b-3 present EDS elemental mapping of the sample cross sections after being subjected to 1000 thermal cycles. Similar to the MEPCM composite sample before the thermal cyclic tests (Fig. 5b), the

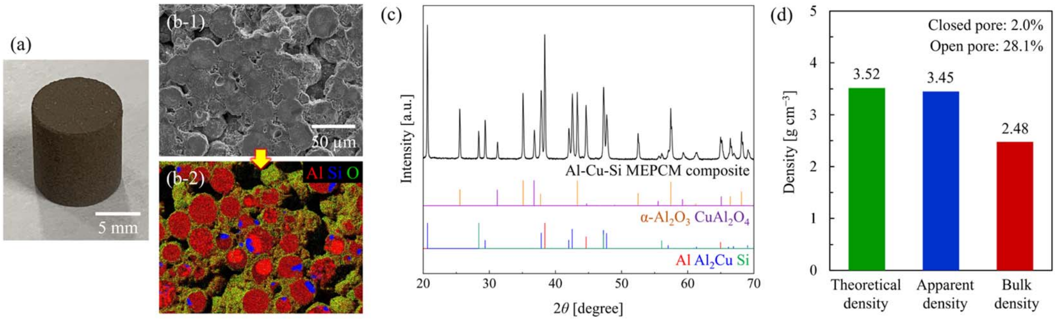

Fig. 5 (a) Photograph of the MEPCM composite sample, (b-1 and b-2) SEM image and EDS elemental mapping of the cross section of the sample, (c) XRD pattern of the composite, and (d) theoretical, apparent, and bulk densities of the composite sample.

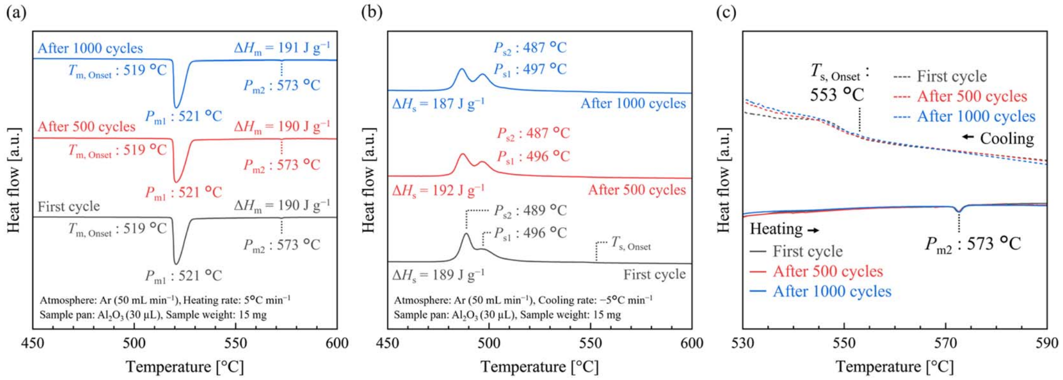

Fig. 6 DSC curves of the MEPCM composite during (a) heating and (b) cooling. (c) Expanded view in the temperature range of 530–590 °C for the first cycle and after 500 and 1000 thermal cycles.

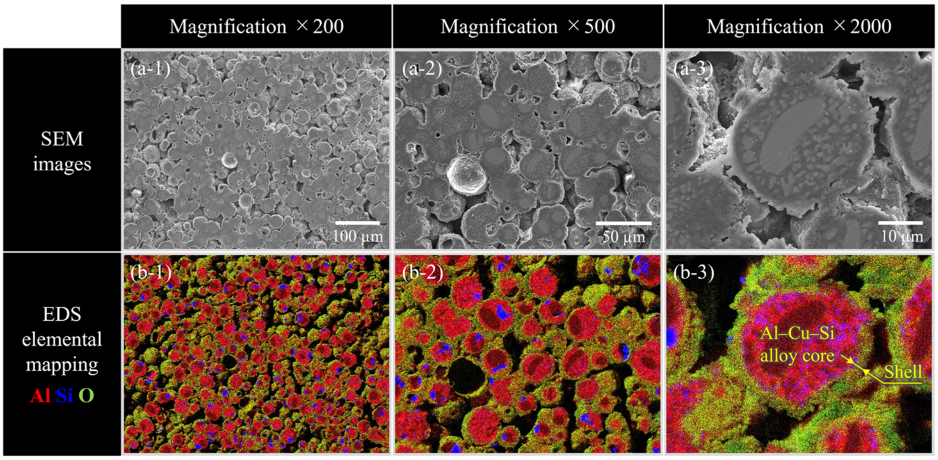

Fig. 7 (a-1–a-3) SEM images and (b-1–b-3) EDS elemental mapping of the sample cross section after 1000 thermal cycles; magnifications: ×200, ×500, and ×2000.

sample cross section exhibited a sintered structure comprising MEPCM with an Al–Cu–Si alloy core and an Al oxide shell. Thus, the composite sample retained its original microcapsule structure even after 1000 thermal cycles. Notably, Cu was not observed in EDS mapping (Fig. 7b-1–b-3) due to limitations in the number of overlapping colors. However, individual elemental mappings including Cu were observed, as shown in Fig. S2. Based on the analytical results obtained using the DSC and SEM-EDS, the developed composite, using Al–Cu–Si-based MEPCM as the base material, possessed excellent thermal cycling durability.

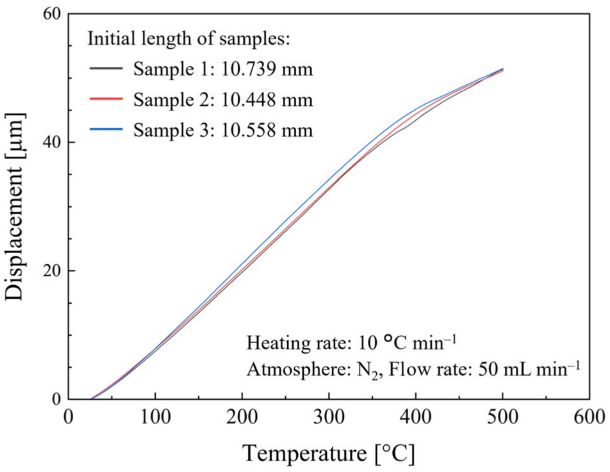

Fig. 8 TMA curves of the Al–Cu–Si MEPCM composite samples.

3.3 Thermophysical properties

Fig. 8 presents the TMA curves of the Al–Cu–Si MEPCM composite samples. The samples exhibited monotonic thermal expansion with increasing temperature. Table 1 presents the average α_{CLTE} values for the MEPCM composite sample at 50–500 °C in intervals of 50 °C. α_{CLTE} remained almost constant at 10.6–12.3 × 10^{-6} °C^{-1} in the temperature range of 50–350 °C. Conversely, in the temperature range of 350–500 °C, α_{CLTE} decreased from 11.5 to 6.1 × 10^{-6} °C^{-1}. Table S2 presents the values of α_{CLTE} in the temperature range of 50–500 °C for each of the three TMA measurements shown in Fig. 8. A discussion of

Table 1 Temperature dependence of the linear thermal expansion coefficient for Al–Cu–Si MEPCM composite samples (average values of measurements for the three samples shown in Fig. 8a)

Temperature [°C]	Liner thermal expansion coefficient, α_{CLTE} [10^{-6} °C^{-1}]
50–100	10.6
100–150	11.6
150–200	12.1
200–250	12.3
250–300	12.2
300–350	11.5
350–400	9.4
400–450	7.1
450–500	6.1

the thermal expansion characteristics of this system is provided in Section 4.2.

Fig. 9a and b present the thermal diffusivity and specific heat and thermal conductivity of the Al–Cu–Si MEPCM composite sample, respectively. In addition, Table S3 presents the values of the thermophysical components plotted in Fig. 9. The thermal diffusivity of the composite samples gradually decreased from 0.0277 to 0.0140 $\mathrm{cm^2\ s^{-1}}$ between 300 and 500 °C, where the MEPCM core alloy remained in its solid phase. Conversely, the specific heat increased from 0.96 to 1.18 J $\mathrm{g^{-1}\ K^{-1}}$ over this temperature range. Upon exceeding the melting point of the MEPCM core alloy at 520 °C, the thermal diffusivity, which decreased up to 500 °C, improved and reached 0.178 at both 550 and 600 °C. The increase in specific heat observed below the melting point stabilized or slightly decreased when the temperature exceeded the melting point, reaching 1.22 and 1.11 at 550 and 600 °C, respectively. Similarly, the experimental thermal conductivity (k_{ex}; Fig. 9b) exhibited a change in temperature dependence beyond the melting point. The value of k_{ex} gradually decreased from 6.6 to 4.1 W $\mathrm{m^{-1}\ K^{-1}}$ between 300 and 500 °C. However, when heated from 500 °C to above the melting point of the MEPCM core alloy at 550 °C, the value of k_{ex} increased from 4.1 to 5.3 W $\mathrm{m^{-1}\ K^{-1}}$. The experimental results regarding the thermal conductivity are discussed in Section 4.3 in comparison with the estimated effective thermal conductivity.

3.4 Compression fracture behavior

Fig. 10a and b present the stress-testing machine displacement curves for the composite samples during compression testing at RT and 500 and 600 °C, respectively. Due to the high-temperature conditions of these tests, displacement measurements on the samples included minor errors originating from the testing machine. As precise correction of these errors is extremely challenging, the horizontal axis (Fig. 10) represented the measured testing machine displacement. The RT compression test results (Fig. 10a) indicated that the three tested samples underwent elastic deformation up to a displacement of approximately 0.14 mm. Subsequently, the samples demonstrated compressive strengths of 86, 81, and 77 MPa, with an average value of 81.3 MPa. After attaining these compressive strengths, the stress rapidly decreased to approximately 33 MPa. Following this drop in stress, one of the samples (sample 3) fractured due to a significant crack at a testing machine displacement of 0.22 mm. The other two samples (samples 1 and 2) exhibited gradual decrease in stress within a testing machine displacement range of 0.22–0.48 mm and fractured when the displacement reached 0.48 mm. However, even in samples 1 and 2 tested at RT, stress decreased sharply immediately after reaching the compressive stress value. Cracking was assumed to have occurred at that point. In the stress–displacement curves obtained at 500 and 600 °C (Fig. 10b), three primary stages of compressive failure behavior were observed. In stage 1, the initial phase of compression deformation, the elastic deformation behavior was evident. The compressive strength of 49 MPa was attained after passing stage 1 at 500 °C, where the MEPCM core was in its solid state. The compressive strength of 31 MPa was attained at 600 °C, where the MEPCM core was in its liquid state. Thus, the compressive strength of the MEPCM composite samples decreased due to the melting of the MEPCM core alloy. In stage 2, after attaining

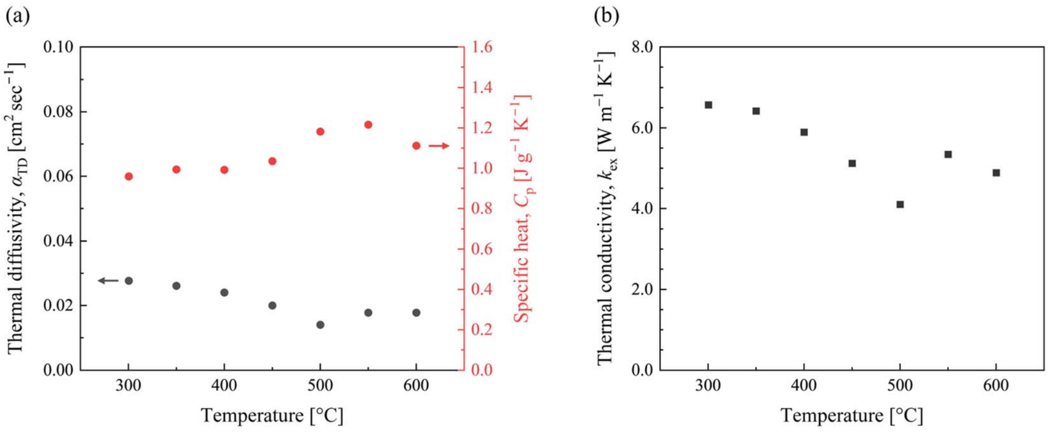

Fig. 9 (a) Thermal diffusivity and specific heat along with (b) thermal conductivity of the Al–Cu–Si MEPCM composite sample (thermal diffusivity: α_{TD}; specific heat: C_p; experimental thermal conductivity: k_{ex}).

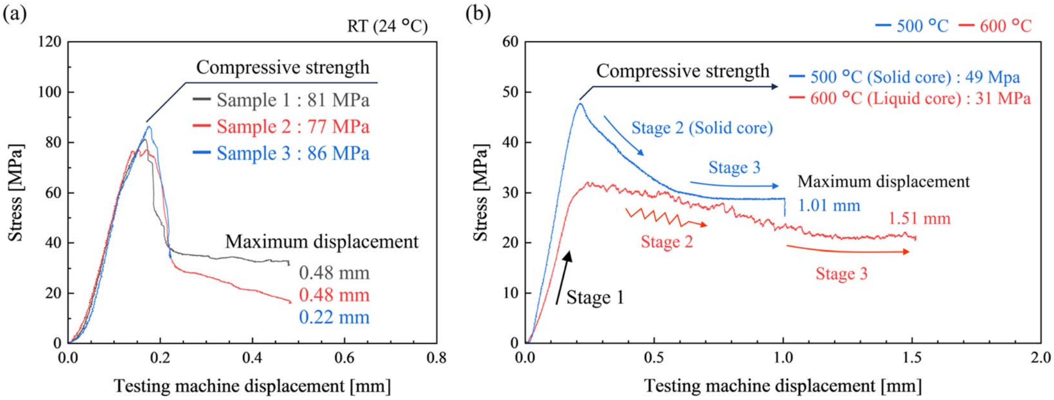

Fig. 10 Stress-testing machine displacement curves for the composite samples during compression tests at (a) room temperature and (b) 500 and 600 °C.

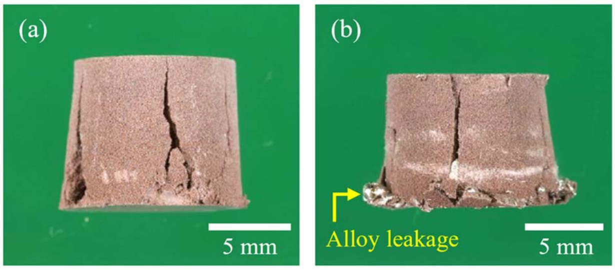

Fig. 11 Photographs of the MEPCM composite samples compressed and fractured at (a) 500 and (b) 600 °C.

the compressive strength, differing behaviors were observed at 500 and 600 °C. At 500 °C, stress gradually decreased with increasing displacement. At 600 °C, stress fluctuated with increasing displacement, demonstrating a gradual decrease overall. Subsequently, in stage 3, both samples at 500 and 600 °C exhibited a reduced rate of stress decrease relative to the increase in displacement, thereby eventually stabilizing. The final stress at the fracture and the maximum displacement were 28.8 MPa and 1.01 mm at 500 °C, and 21.1 MPa and 1.51 mm at 600 °C, respectively. The stress–displacement curves for the compression tests of three specimens at 500, 550, and 600 °C are shown in Fig. S3. At 550 °C, the alloy core of MEPCM was mostly in its liquid phase, resulting in almost identical test results as those at 600 °C. Table S4 presents the maximum load and compressive strength values for all compression tests that were performed.

Fig. 11 presents the photographs of MEPCM composite samples compressed and fractured at 500 and 600 °C. The sample that fractured at 500 °C exhibited only cracks, whereas that fractured at 600 °C showed both cracks and alloy leakage.

Fig. 12 presents the SEM images and EDS elemental mapping of the cross sections of the composite samples after compression testing at RT, 500 °C, and 600 °C. The SEM images in Fig. 12a-1–c-1 show that cracks formed due to compression in all samples, propagating approximately 45° from the bottom edge of the composite samples. The crack orientation was consistent with the general phenomenon in compression

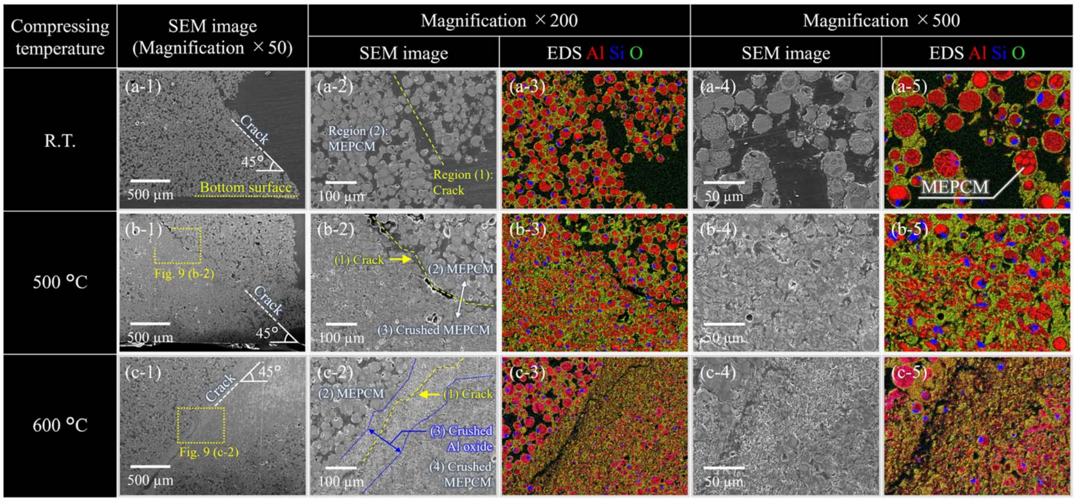

Fig. 12 SEM images and EDS elemental mapping of the cross sections of composite samples after compression testing at (a) RT, (b) 500 °C, and (c) 600 °C.

testing, where maximum shear stress occurs at 45°. As shown in Fig. 12a-2–a-5, the cross section of the sample compressed at RT exhibited two structural features: (1) cracks and (2) Al alloy core/Al oxide shell MEPCM. Notably, MEPCM (the main component of the composite) retained its microcapsule structure in nearly all particles even after the compressive fracture. For the sample compressed at 500 °C, three distinct microstructural regions were observed: (1) cracks, (2) regions where MEPCM retained its structure, and (3) regions where MEPCM was crushed, resulting in a mottled mixture of Al alloy and Al oxide (Fig. 12b-2–b-5). The regions marked as (2) and (3) were separated by the crack region (1). In the sample compressed at 600 °C, four microstructural features were observed: (1) cracks, (2) regions where MEPCM retained its structure, (3) regions surrounding the cracks where mostly Al oxide remained, and (4) regions where MEPCM was crushed, forming a mixture of Al alloy and Al oxide (Fig. 12c-2–c-5). Hence, the cracks in region (1) formed within region (3) after compression at 600 °C.

4. Discussion

4.1 Heat storage properties and thermal cyclic durability

The MEPCM composite fabricated in this study comprised an Al–26.5% Cu–5.4% Si alloy with a near-eutectic composition as PCMs.[73,105] DSC measurements (Fig. 6) revealed a primary melting peak at the eutectic temperature of approximately 520 °C. In addition, a minor endothermic peak observed at 573 °C during melting was attributed to Al oxidation during the composite fabrication process, which altered the alloy composition from the eutectic composition. Fig. S4 presents the phase diagram of Al–$Cu_{0.68403}Si_{0.31597}$, illustrating that a decrease in Al concentration from the eutectic composition increased the liquidus temperature. The shift in alloy composition due to oxidation during Al-alloy-based MEPCM fabrication has been reported in previous studies.[73,84]

As shown in Fig. 6 and 7, the MEPCM composite samples exhibited no significant changes in LHS capacity or structural integrity even after 1000 thermal cycles. When the MEPCM composite samples lacked sufficient durability, structural failure of the microcapsules or alloy oxidation resulted in the deterioration of heat storage performance or leakage of the alloy.[90,93,97] Therefore, the Al–Cu–Si MEPCM composite fabricated in this study exhibited excellent thermal cycling durability.

4.2 Thermal expansion characteristics

The values of α_{CLTE} for α-Al_2O_3 were 4.6 and 7.1×10^{-6} °C^{-1} at 20 and 500 °C,[128] respectively, while those for pure Al were 21.8 and 29.5×10^{-6} °C^{-1} at 50 and 500 °C, respectively.[129] The value for ADC12 (Al–Si–Cu alloy) was 20.1×10^{-6} °C^{-1} from 50 to 200 °C,[130] while that for A6061 (Al–Mg–Si alloy) was 24.3×10^{-6} °C^{-1} from 50 to 500 °C.[131] Therefore, the value of α_{CLTE} for the Al–Cu–Si MEPCM composite was lower than that of conventional Al alloys and approximately equal to that of α-Al_2O_3. Al alloys were dispersed as particles in the internal structure of MEPCM composites, whereas alumina formed a continuous structure. Notably, the thermal expansion coefficient of Al alloys was reduced by incorporating particles with low thermal expansion coefficients, such as alumina and SiC.[129,131,132] In the MEPCM composite, α_{CLTE} decreased as the temperature increased above 350 °C, attributable to the increased solubility of Si in the Al solid solution, which caused the Si crystals to dissolve into the Al solid solution. Si dissolved in the Al solid solution exhibited a smaller volume than Si crystals.[133] Therefore, as the temperature increased, Si dissolved in Al, leading to a decrease in α_{CLTE} for the MEPCM composite. Similar phenomena were reported by Huber *et al.* using A359 (AlSi10Mg) and A356 (AlSi7Mg).[132]

4.3 Effective thermal conductivity

As presented in Section 3.3, the thermal conductivity of the MEPCM composite samples ranged from 4.1 to 6.6 W m^{-1} K^{-1} within the temperature range of 300–600 °C. The average value of 4.8 W m^{-1} K^{-1} was recorded (Fig. 7b). However, the thermal conductivities of the individual components, including the Al–Cu–Si alloy and alumina, were approximately 55–130 W m^{-1} K^{-1} and 8–12 W m^{-1} K^{-1},[105,128] respectively, within the same temperature range. Thus, the presence of significant thermal resistance within the composite samples was observed.

In this section, the effective thermal conductivity of the Al–Cu–Si MEPCM composite is estimated using theoretical models for porous media. This analysis provides insights into the achievable thermal conductivity of the MEPCM composite for future research and development.

The estimated effective thermal conductivity of the MEPCM composite ($k_{\text{eff-comp}}$) can be calculated using the Russell model, as shown in eqn (3):[134,135]

$$\frac{k_{\text{eff-comp.}}}{k_{\mathrm{s}}} = \frac{\varepsilon^{2/3} + \kappa\left(1 - \varepsilon^{2/3}\right)}{\varepsilon^{2/3} - \varepsilon + \kappa\left(1 - \varepsilon^{2/3} + \varepsilon\right)}, \tag{3}$$

where k_{s} is the thermal conductivity of the porous material in the solid phase, κ is the ratio of the thermal conductivities of the solid and gas phases ($\kappa = k_{\mathrm{s}}/k_{\mathrm{g}}$), and ε is the porosity ratio. The thermal conductivity of air[136] (temperature dependence shown in Fig. S5) was used for k_{g}, as air is present in the voids of the porous material. Because the composite fabricated in this study consists of a mixture of the MEPCM and alumina, which acts as a sintering aid, k_{s} is considered to be the thermal conductivity of this mixed material. Therefore, in this study, the thermal conductivity of the microencapsulated structure ($k_{\text{eff-me}}$) is estimated using the predictive method based on the Russell model, as shown in eqn (4):[137]

$$k_{\text{eff-me}} = \frac{\left(1 - 2\dfrac{d}{D}\right)^2 k_{\text{core}} + 4\dfrac{d}{D}\left(1 - \dfrac{d}{D}\right) k_{\text{shell}}}{2\dfrac{d}{D}\left(1 - 2\dfrac{d}{D}\right)^2 k_{\text{core}} + \left(1 - 2\dfrac{d}{D} + 8\left(\dfrac{d}{D}\right)^2\left(1 - \dfrac{d}{D}\right)\right) k_{\text{shell}}}, \tag{4}$$

where d and D represent the shell thickness and overall diameter of the capsule structure, respectively, and k_{shell} and k_{core} denote the thermal conductivities of the shell and core, respectively. Based on the mean particle size and structural observations of the MEPCM powder (Fig. 2), the average particle diameter of the MEPCM was 25.2 μm and the shell thickness was 1.4 μm. In this study, d was determined by assuming that the α-Al_2O_3 added as a sintering aid is included within the shell (a schematic is shown in Fig. S6a). Thus, d and D were determined to be 3.3 and 29.1 μm, respectively. Furthermore, the thermal conductivity of the eutectic Al–Cu–Si alloy (k_{core}) was adopted from a previous study.[105] The thermal conductivity of α-Al_2O_3 (k_{shell}) was calculated based on the study by Smith *et al.*,[138] which investigated thermal resistance at grain boundaries. In this study, the crystal grain size of polycrystalline alumina was assumed to be 0.15 μm, corresponding to the particle size of the α-Al_2O_3 added as a sintering aid. The relationship between the estimated effective thermal conductivity ($k_{\text{eff-me}}$) of the Al–Cu–Si alloy core/α-Al_2O_3 shell-type capsules and temperature (based on this assumption) is shown in Fig. S6b. This figure also presents the thermal conductivities of the Al–Cu–Si alloy and polycrystalline α-Al_2O_3 used in the calculations. Using the values of $k_{\text{eff-me}}$ (*i.e.*, k_s) and k_g, $k_{\text{eff-comp}}$ was estimated using eqn (4) for porosities with ε values of 0.1, 0.2, and 0.3. Fig. 13a illustrates the relationship between $k_{\text{eff-comp}}$ and temperature. According to this estimation, the effective thermal conductivity of the MEPCM composite decreases with increasing temperature and exhibits a discontinuous drop at 520 °C. Fig. S6 shows that this trend corresponds to the reduction in thermal conductivity due to the melting of the Al–Cu–Si alloy. In addition, in the MEPCM composite materials, a lower porosity results in a higher $k_{\text{eff-comp}}$. The $k_{\text{eff-comp}}$ value for $\varepsilon = 0.1$ ranged from 17.1 to 12.1 W m^{-1} K^{-1} over the temperature range of 300–600 °C, which is approximately 1.4 times higher than that for a porosity ratio of 30% ($\varepsilon = 0.3$). However, the $k_{\text{eff-comp}}$ value for $\varepsilon = 0.3$ (Fig. 13a) was more than twice the experimentally obtained thermal conductivity (k_{ex}) for the composite sample with a measured porosity of 30.1% ($\varepsilon = 0.301$) over the temperature range of 300–600 °C. This discrepancy could be due to the low sinterability of the MEPCM and alumina sintering aid powders within the fabricated composite sample, resulting in high thermal resistance at the particle interfaces. Next, the thermal resistance within the solid phase is analyzed using the Kunii–Smith equation, which describes the effective thermal conductivity of a packed bed of granular materials:[139]

$$\frac{k^{\circ}_{\text{eff}}}{k_s} = (1-\varepsilon) \Bigg/ \left(1 + \frac{\varepsilon}{\varepsilon_0}\left(\frac{h_p D_p}{k_s}\right)^{-1}\right), \tag{5}$$

where k°_{eff} represents the effective thermal conductivity in a vacuum, k_s is the thermal conductivity of a solid, ε is the porosity ratio, ε_0 is the maximum porosity ratio, D_p is the particle diameter, and h_p is the heat transfer coefficient between coarse particle contact surfaces. The value of k_s corresponds to the effective thermal conductivity simulating the core–shell structure of the Al–Cu–Si alloy and alumina (Fig. S6). The porosity ε was set at 0.301, while the maximum porosity ε_0 was taken as 0.476, based on the most open packing powder filling fraction.[139] In addition, the term ($h_p D_p/k_s$) represents a dimensionless number indicating the degree of consolidation, referred to as the consolidation parameter. Fig. 13b shows the temperature-dependent curves of k°_{eff} for cases where the ratio of k_{ex} (Fig. 9b) to k_s (Fig. S6) is 0.282 and 0.351. When the average k_{ex} in the 300–500 °C range was used as k_{ex}, the ratio $k_{\text{ex,ave. 300–500}}/k_s$ was 0.282, while for the 550–600 °C range, it was 0.351 ($=k_{\text{ex,ave. 550–600}}/k_s$). From this comparison, it is inferred that the thermal resistance within the composite is lower when the MEPCM core is in the liquid phase compared to the solid phase. Furthermore, the consolidation parameters below and above the melting point of the MEPCM core alloy were found to be 0.65 and 0.82, respectively. This result also suggests that interparticle heat transfer is enhanced when the MEPCM core is in the liquid phase; this improvement could be due to the melting expansion of the MEPCM core alloy, which eliminates the voids within the MEPCM shell and thereby promotes interparticle heat transfer. Consequently, although a decrease in thermal conductivity would typically be expected after melting (according to Fig. 13a), an increase in the experimental value was observed from just below the melting point to above it.

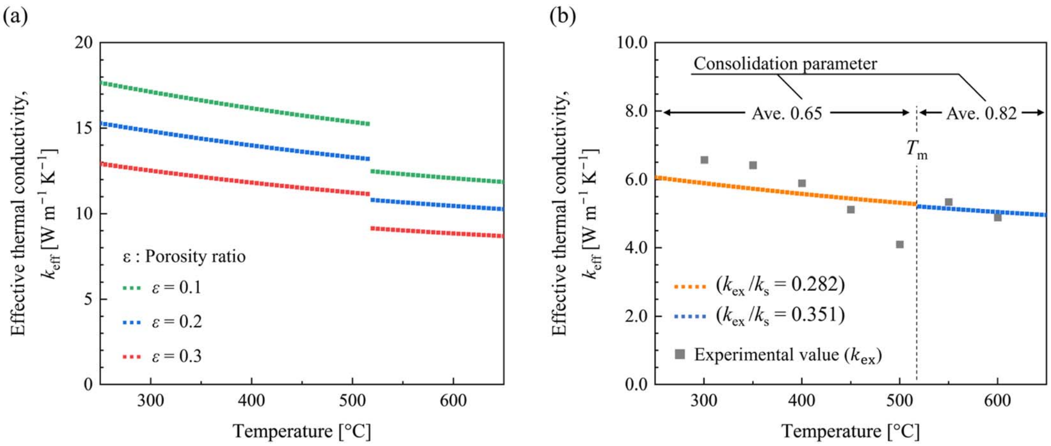

Fig. 13 (a) Effective thermal conductivity of the Al–Cu–Si MEPCM composite for $\varepsilon = 0.1$, 0.2, and 0.3 as estimated by the Russell model; (b) effective thermal conductivity when the average experimental thermal conductivity values for 300–520 °C and 520–600 °C are used in the Kunii–Smith model.

The thermal conductivity of the MEPCM composite sample fabricated in this study (with a porosity of 30.1%) was found to be significantly lower than the estimated $k_{\text{eff-comp}}$ value shown in Fig. 13a. This suggests that the thermal resistance between solid particles is relatively high. To improve the thermal conductivity of the composite, fabrication of a denser material with enhanced sinterability is essential. This may be achieved by adjusting the particle size distribution of the mixed powder containing MEPCM and sintering aids[140,141] or using sintering aids with high sinterability such as TiO_2, La_2O_3, and ZrO_2.[142,143] Even though high-temperature sintering could be employed in MEPCM composites, the possible decrease in latent heat capacity due to the oxidation of the alloy should be carefully avoided. In addition, the Russell model used for the estimation occasionally overestimates the effective thermal conductivity.[144,145] Therefore, this estimation represents one of the possible scenarios that can be achieved using MEPCM composites. To improve the usefulness of this estimation method, further research is required to develop MEPCM composites with different porosities using this method and to fit the estimated values with experimental thermal conductivities.

4.4 Compressive fracture: mechanism and key characteristics

As described in Section 3.4, the cross-sectional structures of the composite samples after compression failure at RT, 500 °C, and 600 °C were distinct. Fig. 14 illustrates the expected failure mechanisms at 500 °C and 600 °C, where stages 1, 2, and 3 correspond to those in Fig. 8. Stage 1 represents the elastic deformation region at both 500 °C and 600 °C, where no irreversible changes (such as MEPCM damage or crack formation) occur. In stage 2 at 500 °C, MEPCM degradation and the formation of microcracks between MEPCM particles occurs, gradually reducing the internal voids. By contrast, in stage 2 at 600 °C, the MEPCM shell is more easily damaged than at 500 °C because the core alloy is in the liquid phase, resulting in the leakage of the alloy from the MEPCM. The stress fluctuations observed in Fig. 8b could be due to the sequential rupture-like breakage of individual MEPCM particles. The difference in the stage 2 mechanism had a significant impact on compressive strength as the compressive strength of the sample at 600 °C was significantly lower than that at 500 °C. Stage 3 at 500 °C results from the breakdown and densification of the microcapsule structure in stage 2, leading to an almost complete elimination of voids. The elimination of voids increases resistance to compressive deformation, resulting in a smaller rate of decrease in stress with increasing displacement (Fig. 10b). The densified area eventually fractures when there is no more allowance for deformation. The crushed, dense MEPCM layer and the final crack formed in this process correspond to the crushed MEPCM (3) and crack areas (1) shown in Fig. 12b-2. Stage 3 at 600 °C forms a region where only Al oxide remains in a significant quantity. This is because the deformation that occurs during stage 2 caused the elimination of voids within the composite and the ejection of the PCM liquid, leaving only the Al oxide composed of the MEPCM shell and the sintering aids. The formation of a dense layer of oxide increases resistance to deformation and reduces the rate of decrease in stress with respect to an increase in displacement. Eventually, the tolerance limit of the dense Al oxide layer is exceeded, leading to fracture. The structures resulting from Al oxide densification and crack initiation correspond to the cracked (1) and crushed (3) Al oxide regions shown in Fig. 12c-2. The region of the crushed MEPCM (4) shown in Fig. 12c-2 is considered to be the microstructure corresponding to the stress fluctuations in Fig. 10b at stage 3.

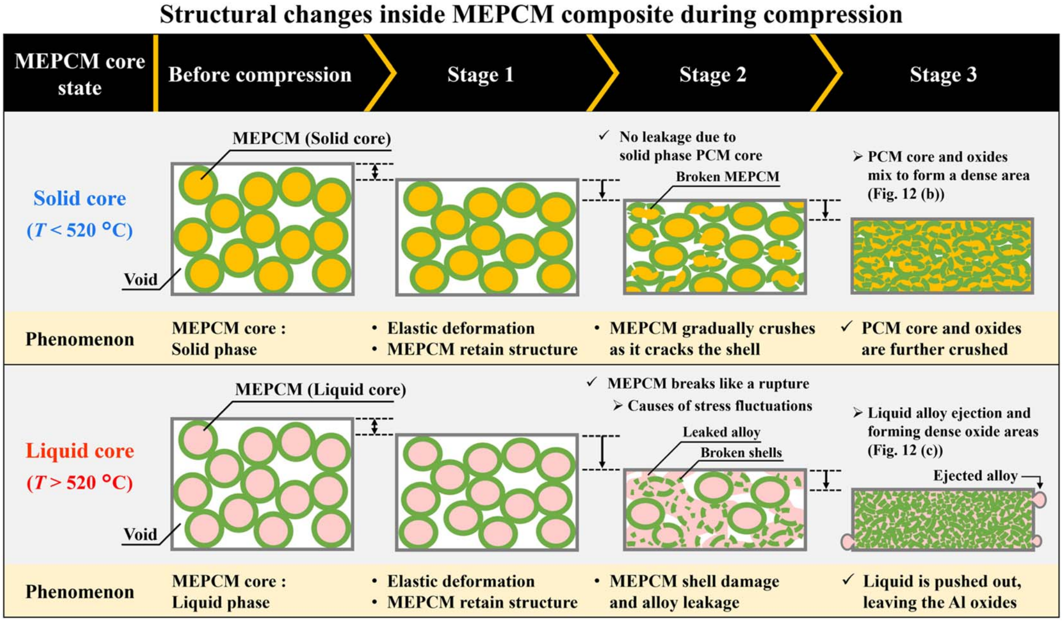

Fig. 14 Schematic of the compressive fracture mechanism of the core alloy in the MEPCM composite during the solid and liquid phases (stages 1, 2, and 3 correspond to the notations in Fig. 10b).

Stage 3 at 600 °C in Fig. 10b shows that the stress fluctuations remain, although they are less prominent than those in stage 2. This suggests that the MEPCM continues to rupture outside of the region of maximum shear stress. In addition, the maximum displacement is greater at 600 °C than at 500 °C because of the ejection of the internal PCM as a liquid at 600 °C (Fig. 11). Finally, the stress–displacement curve at RT (Fig. 10a) shows a sudden drop in stress after reaching the compressive strength, and it is inferred that the specimen cracks at that point.

The compressive fracture mechanism supports the assertion that even when the PCM in the MEPCM composite was in its liquid phase, the liquid was rarely exposed to the surface until the compressive strength was reached. This property serves as a significant advantage because each PCM particle is covered by a ceramic shell. Although molten salt PCM composites have been considered medium-to-high-temperature LHS materials, these composite PCMs are porous materials impregnated with PCM.[114–119] PCM was assumed to seep out onto the surface when compressed while the PCM inside was in a molten state. Such PCM seepage may be reversible to some extent as a microscopic phenomenon occurring at the scale of a single grain. However, in a packed-bed heat storage system, PCM is assumed to spread irreversibly between composite PCMs and onto the surface of the heat storage container. This phenomenon can lead to the agglomeration of composite PCM particles and degradation of the material due to the reaction between the PCM and the container. Therefore, even the composite PCM has limited applications due to concerns regarding its low resistance to thermal ratcheting. Conversely, composites with MEPCM as the main component do not experience PCM wetting and spreading even when in contact with other particles or containers because the PCM is not exposed to the surface if the applied load remains below the compressive strength. Moreover, in our previous studies on Al–Si MEPCM composites in lab-scale to kW h-class bench-scale packed-bed LHS devices, no agglomeration or breakage of heat storage particles was observed even after heat storage and release tests.[94–96]

Table 2 Compressive strength of Al–Cu–Si MEPCM composite samples and existing firebrick and concrete

Material [ref. no.]	Compressive strength [MPa]
Al–Cu–Si MEPCM composite (at RT)[a]	81
Al–Cu–Si MEPCM composite (at 500 °C)[a]	49
Al–Cu–Si MEPCM composite (at 600 °C)[a]	32
Silica brick[b]	44
Alumina brick[c]	65
High alumina brick[d]	83
Chamotte brick[e]	49
Ordinary concrete[147]	18–45
High strength concrete[147]	45–60

[a] Compressive strength of MEPCM composites is the average of three compression tests performed. [b] 95.0% SiO_2–1.0% Al_2O_3–1.0% Fe_2O_3 (bricks for hot stove).[146] [c] 41.6% SiO_2–53.6% Al_2O_3–1.5% Fe_2O_3 (for heating furnace).[146] [d] 20% SiO_2–77% Al_2O_3–1% Fe_2O_3 (bricks for hot stove).[146] [e] 58% SiO_2–38% Al_2O_3–2% Fe_2O_3 (bricks for hot stove).[146]

Table 2 presents the compressive strengths of the MEPCM composite samples, conventional refractory materials, and concrete. The compressive strength values of refractory bricks were obtained from typical values for silica brick, alumina brick, high-alumina brick, and chamotte brick, which are used in practical applications.[146] For concrete, the compressive strength values of ordinary and high-strength concrete were taken from the Japanese Industrial Standards for ready-mixed concrete (JIS 5308: 2024).[147] The compressive strengths of the composite sample at RT (81 MPa) and 500 °C (49 MPa) were equal to or higher than those of the silica brick (44 MPa), alumina brick (65 MPa), high-alumina brick (83 MPa), chamotte brick (49 MPa), and high-strength concrete (45–60 MPa). Furthermore, even at 600 °C, when the core alloy of the composite sample was in its liquid state, its compressive strength (32 MPa) remained comparable to that of ordinary concrete (18–45 MPa). These findings indicated that although the compressive strength of the Al–Cu–Si MEPCM composite decreased at higher temperatures, it retained a strength that was comparable to that of ordinary concrete even when its internal structure was in a liquid state. Therefore, the composite sample was considered to exhibit sufficiently high compressive strength for use as a heat storage material. This discussion is significant for the future scaling-up of packed-bed LHS and thermal management systems, which have previously been explored MEPCM composites.[41,42,94–96]

4.5 Comparison with conventional sensible heat storage materials

Fig. 15 presents the volume-based heat storage densities at ΔT = 100 and 200 °C for conventional SHS materials such as

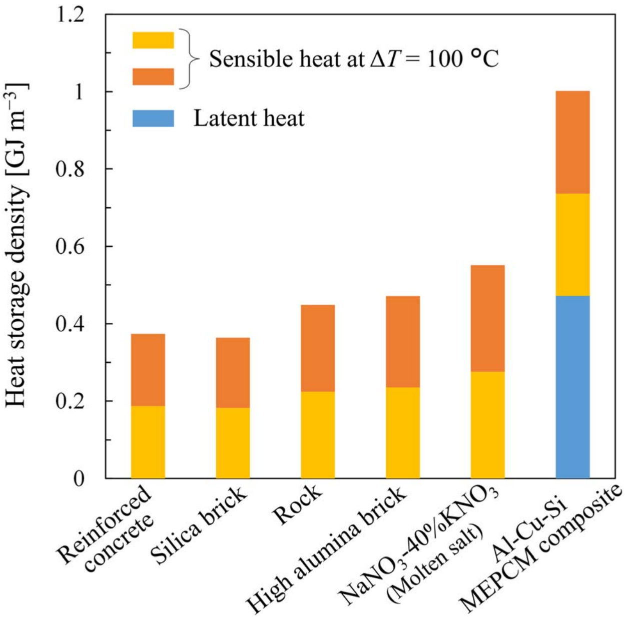

Fig. 15 Heat storage density per unit volume at ΔT = 100 and 200 °C for conventional solid and liquid sensible heat storage materials and Al–Cu–Si MEPCM composite.

Table 3 Density, specific heat, and thermal conductivity of the heat storage materials shown in Fig. 15

Material (at temperature) [ref. no.]	Density [kg m^{-3}]	Specific heat [kJ kg^{-1} K^{-1}]	Thermal conductivity [W m^{-1} K^{-1}]
Reinforced concrete (ave. at 200–400 °C)[148]	2200	0.85	1.5
Silica brick (ave. at 200–700 °C)[148]	1820	1.0	1.5
Rock[149]	2240	1.0	—
High alumina brick (1027 °C)[136]	2200	1.07	1.7
$NaNO_3$–40% KNO_3 (molten salt) (300 °C)[150]	1730	1.54	0.6
Al–Cu–Si MEPCM composite (ave. 300–600 °C)	2480	1.07	5.5

reinforced concrete, silica brick, rock, high-alumina brick, molten nitrate, and the Al–Cu–Si MEPCM composite fabricated in this study. Table 3 presents the density, specific heat, and thermal conductivity of each of the heat storage materials shown in Fig. 15.[136,148–150] When the latent heat component of the MEPCM composite was combined with a sensible heat component at $\Delta T = 100$ °C or 200 °C, the resulting heat storage density reached 0.74 and 1.0 GJ m^{-3}, respectively. Assuming $\Delta T = 100$ or 200 °C, the MEPCM composite exhibited a heat storage density that was 3–4 or 2–3 times higher than that of other SHS materials, respectively. Furthermore, as shown in Table 3, the thermal conductivity of the MEPCM composite was higher than that of conventional SHS materials. Therefore, the MEPCM composite can facilitate the design of heat storage systems with a higher heat storage density, compactness, and more rapid heat exchange compared to conventional SHS materials.

It should be noted that the Al–Cu–Si MEPCM composite was compared with conventional SHS materials because these materials are generally used in similar temperature ranges for heat storage applications. Previously developed alloy-based LHS composites include the SnBi58 alloy and Al–Si alloy-based phase change composites, which exhibit phase change temperatures of 150 and 577 °C, respectively.[90,100] Because the operating temperatures of these materials differ from that of the material investigated in this study, this comparison is provided only for reference. Fig. S7 shows the volume-based heat storage densities of these materials at $\Delta T = 100$ °C. The SnBi58 alloy and Al–Si alloy-based MEPCM composites exhibited heat storage densities of 0.40 and 0.56 GJ m^{-3}, respectively. As the Al–Cu–Si MEPCM composite developed in this study has a heat storage density of 0.74 GJ m^{-3} at $\Delta T = 100$ °C, this verifies that this material exhibits a high heat storage density compared to alloy-based LHS materials.

5. Conclusion

In this study, Al–Cu–Si MEPCM composites were developed as medium-to-high-temperature LHS materials, and their structures, thermophysical properties, heat storage performance, thermal cycling durability, and compressive fracture characteristics were evaluated. This study is the first to investigate the compressive strength and fracture mechanism of LHS composites under high-temperature conditions where the PCM exists in a liquid state. The key findings of this study are summarized as follows:

- The Al–Cu–Si MEPCM composite was fabricated as a sintered structure in which the MEPCM, comprising an Al–Cu–Si alloy core and an Al oxide shell, was co-sintered with alumina powder serving as a sintering aid. The resulting composite exhibited a bulk density of 2.48 g cm^{-3} and a porosity of 30.1%.
- The composite exhibited a specific heat of 0.96–1.22 J g^{-1} K^{-1} and a thermal conductivity of 4.1–6.6 W m^{-1} K^{-1} over a temperature range of 300–600 °C. Under heat storage conditions with a temperature difference (ΔT) of 200 °C, the composite achieved a heat storage density of approximately 1.0 GJ m^{-3}, which was two-to-three times that of conventional SHS materials.
- The MEPCM composite retained its structural integrity after undergoing 1000 thermal cycles, with no observed changes in its phase change temperature or latent heat capacity.
- Even at high temperatures where the PCM existed in a liquid state, the MEPCM composite prevented the PCM from being exposed at the surface until its compressive strength limit was reached. This behavior represents a distinctive advantage over conventional composite PCMs, which typically comprise porous media impregnated with PCM and are more prone to leakage under similar conditions.
- At RT, the MEPCM composite exhibited a compressive strength of 81 MPa, which was comparable to or greater than that of silica bricks, alumina bricks, and high-strength concrete. Remarkably, even at 600 °C—when the internal Al alloy was in a molten state—the composite retained a compressive strength of 32 MPa, which was comparable to that of ordinary concrete.

Future research will focus on further densifying the MEPCM composite to enhance its thermal conductivity, heat storage density, and mechanical strength. Moreover, repeated thermal deformation tests within the elastic deformation range of MEPCM composites, which were not assessed in the present compression tests, are required to further investigate the durability of MEPCM composites against thermal ratcheting. Considering the applications of these materials, packed-bed heat storage and heat exchanger systems incorporating Al–Cu–Si MEPCM composites should be investigated, and thermal management technologies that use latent heat to maintain temperature-fluctuating processes at a constant phase change temperature should be developed.

Author contributions

Yuto Shimizu: investigation, data curation, formal analysis, visualization, funding acquisition, writing – original draft, writing – review & editing. Takahiro Kawaguchi: writing – review & editing, data curation. Joshua Chidiebere Mba: writing – review & editing, data curation. Tomokazu Nakamura: writing – review & editing, data curation. Keita Tanahashi: writing – review & editing, data curation. Melbert Jeem: writing – review & editing, data curation. Takahiro Nomura: conceptualization, funding acquisition, methodology, project administration, supervision, writing – review & editing.

Conflicts of interest

The authors declare that they have no known competing financial interests or personal relationships that could have appeared to influence the work reported in this paper.

Data availability

The authors confirm that the data supporting the findings of this study are available within the article or its SI.

Supplementary information, which includes supplementary figures and tables, is available. See DOI: **https://doi.org/10.1039/d5ta03994k**.

Acknowledgements

This paper was partially supported by the JSPS KAKENHI (grant number JP22K18993 and JP23KJ0050) and the Light Metal Educational Foundation of Japan. A part of this work was conducted at Hokkaido University, supported by the "Nanotechnology Platform" Program of the Ministry of Education, Culture, Sports, Science and Technology (MEXT), Japan.

References

1 E. T. Sayed, A. G. Olabi, A. H. Alami, A. Radwan, A. Mdallal, A. Rezk and M. A. Abdelkareem, *Energies*, 2023, **16**, 1415.
2 M. C. Argyrou, P. Christodoulides and S. A. Kalogirou, *Renewable Sustainable Energy Rev.*, 2018, **94**, 804–821.
3 W.-D. Steinmann, *Renewable Sustainable Energy Rev.*, 2017, **75**, 205–219.
4 Q. Yong, Y. Tian, X. Qian and X. Li, *Appl. Therm. Eng.*, 2022, **215**, 119048.
5 F. Kosaka, T. Yamaguchi, Y. Ando, T. Mochizuki, H. Takagi, K. Matsuoka and K. Kuramoto, *Int. J. Hydrogen Energy*, 2021, **46**, 4116–4125.
6 Y. Li, J. An, S. Wang, Z. Geng and H. Dong, *Adv. Powder Technol.*, 2024, **35**, 104671.
7 S. Sakamoto, T. Matsuoka and Y. Nakamura, *Catal. Lett.*, 2020, **150**, 2928–2936.
8 D. Sun and D. S. Simakov, *J. CO2 Util.*, 2017, **21**, 368–382.
9 H. Koide, A. Gunji, M. Sugimasa, T. Kawaguchi, C. Tamzysi and T. Nomura, *Appl. Energy*, 2025, **380**, 124942.
10 T. Takahashi, H. Koide, H. Sakai, D. Ajito, A. Kurniawan, Y. Kunisada and T. Nomura, *Sci. Rep.*, 2021, **11**, 7539.
11 C. Tamzysi, T. Takahashi, Y. Kunisada, A. Kurniawan and T. Nomura, *Chem. Eng. J.*, 2025, **506**, 159753.
12 V. Dieterich, A. Buttler, A. Hanel, H. Spliethoff and S. Fendt, *Energy Environ. Sci.*, 2020, **13**, 3207–3252.
13 Y. Liu, O. Ersen, C. Meny, F. Luck and C. Pham-Huu, *ChemSusChem*, 2014, **7**, 1218–1239.
14 A. O. Odunsi, T. S. O'Donovan and D. A. Reay, *Appl. Therm. Eng.*, 2016, **93**, 1377–1393.
15 M. Promsen, K. Selvam, Y. Komatsu, A. Sciazko, S. Kaneko and N. Shikazono, *Energy Convers. Manage.*, 2022, **255**, 115309.
16 S. Santhanam, M. P. Heddrich, M. Riedel and K. A. Friedrich, *Energy*, 2017, **141**, 202–214.
17 G. Xiao, A. Sun, H. Liu, M. Ni and H. Xu, *Appl. Energy*, 2023, **331**, 120383.
18 N. Javanshir, S. Syri, S. Tervo and A. Rosin, *Energy*, 2023, **266**, 126423.
19 J. Ramsebner, R. Haas, A. Ajanovic and M. Wietschel, *Wiley Interdiscip. Rev.: Energy Environ.*, 2021, **10**, e396.
20 E. Zeyen, M. Victoria and T. Brown, *Nat. Commun.*, 2023, **14**, 3743.
21 T. Liang, A. Vecchi, K. Knobloch, A. Sciacovelli, K. Engelbrecht, Y. Li and Y. Ding, *Renewable Sustainable Energy Rev.*, 2022, **163**, 112478.
22 L. Seyitini, B. Belgasim and C. C. Enweremadu, *J. Energy Storage*, 2023, **62**, 106919.
23 A. J. Carrillo, J. González-Aguilar, M. Romero and J. M. Coronado, *Chem. Rev.*, 2019, **119**, 4777–4816.
24 H. M. Ali, T.-u. Rehman, M. Arıcı, Z. Said, B. Duraković, H. I. Mohammed, R. Kumar, M. K. Rathod, O. Buyukdagli and M. Teggar, *Prog. Energy Combust. Sci.*, 2024, **100**, 101109.
25 T. Nomura, N. Okinaka and T. Akiyama, *ISIJ Int.*, 2010, **50**, 1229–1239.
26 B. Zalba, J. M. Marín, L. F. Cabeza and H. Mehling, *Appl. Therm. Eng.*, 2003, **23**, 251–283.
27 Y. Zhao, C. Y. Zhao, C. N. Markides, H. Wang and W. Li, *Appl. Energy*, 2020, **280**, 115950.
28 S. Wang, K. Lei, Z. Wang, H. Wang and D. Zou, *Chem. Eng. J.*, 2022, **438**, 135559.
29 Y. Ouyang, Y. Luo, X. Gao, H. Gao, G. Wang and X. Shu, *Chin. J. Catal.*, 2024, **60**, 128–157.
30 X. Hu, X. Gong, F. Zhu, X. Xing, Z. Li and X. Zhang, *Renewable Energy*, 2023, **212**, 227–237.
31 W. Hua, L. Zhang and X. Zhang, *J. Mol. Liq.*, 2021, **340**, 117183.
32 Z.-w. Li, L.-c. Lv and J. Li, *Int. J. Heat Mass Transfer*, 2016, **98**, 550–557.
33 G. Liu, K. Shang, S. Chen and J. Shen, *Compos. Sci. Technol.*, 2025, 111120, in press.
34 R. Fan, N. Zheng and Z. Sun, *Int. J. Heat Mass Transfer*, 2021, **166**, 120753.
35 R. Kizilel, R. Sabbah, J. R. Selman and S. Al-Hallaj, *J. Power Sources*, 2009, **194**, 1105–1112.
36 Z. Ling, F. Wang, X. Fang, X. Gao and Z. Zhang, *Appl. Energy*, 2015, **148**, 403–409.
37 Z. Ling, Z. Zhang, G. Shi, X. Fang, L. Wang, X. Gao, Y. Fang, T. Xu, S. Wang and X. Liu, *Renewable Sustainable Energy Rev.*, 2014, **31**, 427–438.

38 S. Mousavi, A. Zadehkabir, M. Siavashi and X. Yang, *Appl. Energy*, 2023, **334**, 120643.

39 M. Safdari, R. Ahmadi and S. Sadeghzadeh, *Energy*, 2020, **193**, 116840.

40 E. Shengxin, Y. Cui, Y. Liu and H. Yin, *Energy*, 2023, **282**, 128805.

41 K. Takizawa, D. A. R. Sanjeew, N. Yagihashi, K. Mimura, Y. Shimizu, M. Jeem and T. Nomura, *Chem. Eng. J.*, 2025, **504**, 158558.

42 C. Tamzysi, Y. Shimizu, T. Nakamura, M. Jeem, K. Tanahashi, T. Kawaguchi, K. Mimura, A. Kurniawan and T. Nomura, *React. Chem. Eng.*, 2025, **10**, 593–604.

43 H. Mehling, *Appl. Sci.*, 2023, **13**, 8682.

44 Q. Zhang, Y. Li, C. Liu, X. Wu, X. Zhang, J. Song, Y. Mao and K. Yuan, *J. Mater. Chem. A*, 2024, **12**, 32526–32547.

45 S. Zhu, M. T. Nguyen and T. Yonezawa, *Nanoscale Adv.*, 2021, **3**, 4626–4645.

46 C. Shi, M. Xu, X. Guo, S. Zhu and D. Zou, *Adv. Funct. Mater.*, 2025, **35**, 2412914.

47 X. Lu, R. Qian, X. Xu, M. Liu, Y. Liu and D. Zou, *Nano Energy*, 2024, **124**, 109520.

48 W. Su, J. Darkwa and G. Kokogiannakis, *Renewable Sustainable Energy Rev.*, 2015, **48**, 373–391.

49 N. P. Pasarkar, M. Yadav and P. A. Mahanwar, *J. Polym. Res.*, 2023, **30**, 13.

50 Y. Sheikh, M. O. Hamdan and S. Sakhi, *J. Energy Storage*, 2023, **72**, 108472.

51 J. Lee and B. Jo, *Sol. Energy Mater. Sol. Cells*, 2021, **222**, 110954.

52 J. Li, L. Li, H. Wang, X. Zhu, Y. Chen and L. Jia, *Energy Technol.*, 2020, **8**, 2000550.

53 S. Mo, B. Xiao, B. Mo, J. Chen, L. Jia, Z. Wang and Y. Chen, *Energy Fuels*, 2023, **37**, 7490–7500.

54 S. Park and B. Jo, *Sol. Energy Mater. Sol. Cells*, 2024, **272**, 112905.

55 H. Zhang, D. Shin and S. Santhanagopalan, *Renewable Energy*, 2019, **134**, 1156–1162.

56 T. Nomura, C. Zhu, N. Sheng, G. Saito and T. Akiyama, *Sci. Rep.*, 2015, **5**, 9117.

57 K. Kashiyama, T. Kawaguchi, K. Dong, H. Sakai, N. Sheng, A. Kurniawan and T. Nomura, *Energy Storage*, 2020, **2**, e177.

58 K. Dong, T. Kawaguchi, Y. Shimizu, H. Sakai and T. Nomura, *ACS Omega*, 2022, **7**, 28313–28323.

59 K. Ishii, K. Kawayama and K. Fumoto, *J. Energy Storage*, 2023, **59**, 106426.

60 M. Jeem, R. Ishida, M. Kondo, Y. Shimizu, T. Kawaguchi, K. Dong, A. Kurniawan, Y. Kunisada, N. Sakaguchi and T. Nomura, *ACS Appl. Mater. Interfaces*, 2024, **16**, 3509–3519.

61 J. Bao, D. Zou, S. Zhu, Q. Ma, Y. Wang and Y. Hu, *Chem. Eng. J.*, 2021, **415**, 128965.

62 K. Lei, J. Bao, X. Zhao, H. Wang and D. Zou, *Chem. Eng. J.*, 2022, **446**, 137020.

63 J. Lu, N. Sheng and C. Zhu, *Sol. Energy Mater. Sol. Cells*, 2022, **239**, 111652.

64 N. Sheng, H. Guo, C. Zhu and Z. Rao, *J. Energy Storage*, 2022, **56**, 106069.

65 N. Sheng, J. Lu, J. Hu, R. Zhu, L. Fadillah, C. Wang, C. Zhu, Z. Rao and H. Habazaki, *Chem. Eng. J.*, 2021, **420**, 129906.

66 C.-C. Lai, S.-M. Lin, Y.-D. Chu, C.-C. Chang, Y.-L. Chueh and M.-C. Lu, *Nano Energy*, 2016, **25**, 218–224.

67 S. Wang, X. Zhao, Z. Wang, Y. Zhang, H. Wang and D. Zou, *J. Clean. Prod.*, 2023, **417**, 138058.

68 T.-H. Hsu, C.-H. Chung, F.-J. Chung, C.-C. Chang, M.-C. Lu and Y.-L. Chueh, *Nano Energy*, 2018, **51**, 563–570.

69 T. Kawaguchi, T. Nakamura, M. Kondo, J. C. Mba, K. Dong, Y. Shimizu, M. Jeem and T. Nomura, *Chem. Eng. J.*, 2024, **498**, 154782.

70 T. Kawaguchi, H. Sakai, R. Ishida, Y. Shimizu, A. Kurniawan and T. Nomura, *J. Energy Storage*, 2022, **55**, 105577.

71 T. Kawaguchi, H. Sakai, N. Sheng, A. Kurniawan and T. Nomura, *Appl. Energy*, 2020, **276**, 115487.

72 Q. Li, X. Ma, X. Zhang, J. Ma, X. Hu and Y. Lan, *Mater. Lett.*, 2022, **308**, 131208.

73 Y. Shimizu, S. Cho, T. Kawaguchi, K. Tanahashi, K. Dong, T. Nakamura, A. Kurniawan, M. Jeem and T. Nomura, *J. Energy Storage*, 2024, **75**, 109535.

74 C. Zhou, L. Jiang, Z. Gu, C. Wang, L. He, L. Huang, Z. Li and K. Li, *Chem. Eng. J.*, 2023, **471**, 144610.

75 N. Sheng, C. Zhu, G. Saito, T. Hiraki, M. Haka, Y. Hasegawa, H. Sakai, T. Akiyama and T. Nomura, *J. Mater. Chem. A*, 2018, **6**, 18143–18153.

76 J. C. Mba, H. Sakai, K. Dong, Y. Shimizu, M. Kondo, T. Nakamura, M. Jeem and T. Nomura, *J. Energy Storage*, 2024, **94**, 112066.

77 T. Nomura, J. Yoolerd, N. Sheng, H. Sakai, Y. Hasegawa, M. Haga, G. Saito and T. Akiyama, *Sol. Energy Mater. Sol. Cells*, 2018, **187**, 255–262.

78 R. Qian, K. Weng, M. Liu, L. Huang and D. Zou, *Chem. Eng. J.*, 2024, **496**, 153929.

79 N. Sheng, C. Zhu, H. Sakai, Y. Hasegawa, T. Akiyama and T. Nomura, *Sol. Energy Mater. Sol. Cells*, 2019, **200**, 109925.

80 K. Wang, T. Zhang, T. Wang, C. Xu, F. Ye and Z. Liao, *Chem. Eng. J.*, 2022, **436**, 135054.

81 H. Wei, C. Wang, S. Yang, J. Han, M. Yang, J. Zhang, Y. Lu and X. Liu, *Chem. Eng. J.*, 2020, **391**, 123539.

82 J. Zhang, M. Zhang, H. Li, H. Gu, D. Chen, C. Zhang, Y. Tian, E. Wang and Q. Mu, *J. Mater. Sci. Technol.*, 2024, **176**, 48–56.

83 J. Zhang, M. Zhang, H. Gu, H. Li, A. Huang, S. Yang, T. Long and X. Zhang, *Chem. Eng. J.*, 2024, **485**, 150119.

84 Y. Shimizu, T. Kawaguchi, H. Sakai, K. Dong, A. Kurniawan and T. Nomura, *Sol. Energy Mater. Sol. Cells*, 2022, **246**, 111874.

85 T. Kawaguchi, J. Yoolerd, H. Sakai, Y. Shimizu, A. Kurniawan and T. Nomura, *Sol. Energy Mater. Sol. Cells*, 2022, **237**, 111540.

86 Q. Li, X. Ma, X. Zhang, J. Ma, J. Liu, X. Hu and Y. Lan, *J. Alloys Compd.*, 2021, **888**, 161606.

87 T. Nomura, J. Yoolerd, N. Sheng, H. Sakai, Y. Hasegawa, M. Haga and T. Akiyama, *Sol. Energy Mater. Sol. Cells*, 2019, **193**, 281–286.

88 K. Li, X. Cheng, N. Li, X. Zhu, Y. Wei, K. Zhai and H. Wang, *J. Mater. Chem. A*, 2017, **5**, 24232–24246.

89 M. Aoki, M. Jeem, Y. Shimizu, T. Kawaguchi, M. Kondo, T. Nakamura, C. Fushimi and T. Nomura, *Mater. Adv.*, 2024, **5**, 675–684.

90 T. Kawaguchi, M. Jeem, A. Kurniawan, K. Dong, M. Kondo, Y. Sato, T. Nakamura and T. Nomura, *J. Energy Storage*, 2024, **75**, 109635.

91 T. Kawaguchi, H. Sakai, Y. Shimizu, K. Dong, A. Kurniawan and T. Nomura, *ISIJ Int.*, 2022, **62**, 2567–2572.

92 T. Kawaguchi, Y. Shimizu, K. Dong, A. Kurniawan and T. Nomura, *Energy Storage*, 2024, **6**, e493.

93 H. Sakai, N. Sheng, A. Kurniawan, T. Akiyama and T. Nomura, *Appl. Energy*, 2020, **265**, 114673.

94 H. Koide, A. Kurniawan, T. Takahashi, T. Kawaguchi, H. Sakai, Y. Sato, J. N. Chiu and T. Nomura, *Energy*, 2022, **238**, 121746.

95 A. Kurniawan, R. Tsukiashi, Y. Shimizu, Y. Sato, T. Nakamura, J. N. Chiu and T. Nomura, *Appl. Therm. Eng.*, 2025, **259**, 124696.

96 T. Nakamura, Y. Sato, L. Shan, J. N. Chiu, S. Fujii and T. Nomura, Experimental Study of a Bench Scale Packed-bed Latent Heat Storage Unit with Al-Si based PCM pellets, *Proceedings of the 16th IEA ES TCP International Conference on Energy Storage*, Lyon, France, 2024.

97 Q. Ma, D. Zou, Y. Wang and K. Lei, *Ceram. Int.*, 2021, **47**, 24240–24251.

98 X. Yao, Y. Chang, H. Gu, J. Guo and D. Zou, *Chem. Eng. J.*, 2023, **477**, 146967.

99 Z. Wang, K. Lei, S. Wang, F. Wang, Y. Zhang and D. Zou, *Ceram. Int.*, 2023, **49**, 19136–19148.

100 Z. Wang, M. Liu, Y. Chang, J. Guo and D. Zou, *Ceram. Int.*, 2023, **49**, 36560–36571.

101 Z. Wang, S. Zhu, X. Zhao, L. Huang and D. Zou, *Int. J. Therm. Sci.*, 2022, **176**, 107478.

102 S. P. Vudata and D. Bhattacharyya, *Int. J. Heat Mass Transfer*, 2021, **181**, 122025.

103 Z. Alipour, V. B. Borugadda, H. Wang and A. K. Dalai, *Chem. Eng. J.*, 2023, **452**, 139416.

104 M. Li, Z. Sun and Y. H. Hu, *J. Mater. Chem. A*, 2021, **9**, 12495–12520.

105 A. Rawson, C. Villada, M. Kolbe, V. Stahl and F. Kargl, *Energy Storage*, 2022, **4**, e299.

106 A. H. Alami, A. G. Olabi, A. Mdallal, A. Rezk, A. Radwan, S. M. A. Rahman, S. K. Shah and M. A. Abdelkareem, *Int. J. Thermofluids*, 2023, **18**, 100340.

107 E. González-Roubaud, D. Pérez-Osorio and C. Prieto, *Renewable Sustainable Energy Rev.*, 2017, **80**, 133–148.

108 Y. Tian and C.-Y. Zhao, *Appl. Energy*, 2013, **104**, 538–553.

109 D. L. Barth, J. E. Pacheco, W. J. Kolb and E. E. Rush, *J. Sol. Energy Eng.*, 2002, **124**, 170–175.

110 U. Herrmann, B. Kelly and H. Price, *Energy*, 2004, **29**, 883–893.

111 P. Speidel, B. Kelly, M. Prairie, J. Pacheco, R. Gilbert and H. Reilly, *J. Phys. IV*, 1999, **9**, Pr3-181–Pr3-187.

112 V. Novotny, V. Basta, P. Smola and J. Spale, *Energies*, 2022, **15**, 647.

113 A. Vecchi, K. Knobloch, T. Liang, H. Kildahl, A. Sciacovelli, K. Engelbrecht, Y. Li and Y. Ding, *J. Energy Storage*, 2022, **55**, 105782.

114 J. Liu, J. Xu, Z. Su, Y. Zhang and T. Jiang, *Sol. Energy Mater. Sol. Cells*, 2023, **251**, 112114.

115 H. Yang, W. Zhang, Y. Zhu, Y. Shao, Y. Shao and X. Zhang, *J. Energy Storage*, 2022, **56**, 106047.

116 F. Jiang, Z. Ge, X. Ling, D. Cang, L. Zhang and Y. Ding, *Renewable Energy*, 2021, **179**, 327–338.

117 F. Jiang, L. Zhang, D. Cang, X. Ling and Y. Ding, *Ceram. Int.*, 2021, **47**, 26301–26309.

118 L. Sang and Y. Xu, *J. Energy Storage*, 2020, **31**, 101611.

119 G. Xu, G. Leng, C. Yang, Y. Qin, Y. Wu, H. Chen, L. Cong and Y. Ding, *Sol. Energy*, 2017, **146**, 494–502.

120 G. Leng, G. Qiao, Z. Jiang, G. Xu, Y. Qin, C. Chang and Y. Ding, *Appl. Energy*, 2018, **217**, 212–220.

121 Q. Li, L. Cong, X. Zhang, B. Dong, B. Zou, Z. Du, Y. Xiong and C. Li, *Sol. Energy Mater. Sol. Cells*, 2020, **211**, 110511.

122 J. R. Eggers, M. von der Heyde, S. H. Thaele, H. Niemeyer and T. Borowitz, *J. Energy Storage*, 2022, **55**, 105780.

123 E. Garitaonandia, P. Arribalzaga, I. Miguel and D. Bielsa, *Energies*, 2024, **17**, 1515.

124 G. Zanganeh, A. Pedretti, S. Zavattoni, M. Barbato and A. Steinfeld, *Sol. Energy*, 2012, **86**, 3084–3098.

125 V. Dreißigacker, H. Müller-Steinhagen and S. Zunft, *Heat Mass Tran.*, 2010, **46**, 1199–1207.

126 T. Mitterlehner, G. Kartnig and M. Haider, *FME Trans.*, 2020, **48**, 427–431.

127 R. Larsen, T. L. Villadsen, J. K. Mathiesen, K. M. Jensen and E. D. Boejesen, *ChemRxiv*, 2023, preprint, DOI: 10.26434/chemrxiv-2023-k73qz-v2.

128 R. G. Munro, *J. Am. Ceram. Soc.*, 1997, **80**, 1919–1928.

129 S. Elomari, M. D. Skibo, A. Sundarrajan and H. Richards, *Compos. Sci. Technol.*, 1998, **58**, 369–376.

130 Y. Shimizu and T. Nomura, *J. Alloys Compd.*, 2025, **1017**, 179006.

131 S. Elomari, R. Boukhili and D. J. Lloyd, *Acta Mater.*, 1996, **44**, 1873–1882.

132 T. Huber, H. P. Degischer, G. Lefranc and T. Schmitt, *Compos. Sci. Technol.*, 2006, **66**, 2206–2217.

133 E. J. Mittemeijer, P. V. Mourik and T. H. De Keijser, *Philos. Mag. A*, 1981, **43**, 1157–1164.

134 H. W. Russell, *J. Am. Ceram. Soc.*, 1935, **18**, 1–5.

135 M. Matsushita, M. Monde and Y. Mitsutake, *Int. J. Hydrogen Energy*, 2014, **39**, 9718–9725.

136 J. S. o. T. Properties, *Thermophysical Properties Handbook*, Yokendo Co. Ltd., 1st edn, 2008.

137 J. Czyzewski, A. Rybak, K. Gaska, R. Sekula and C. Kapusta, *Materials*, 2020, **13**, 5480.

138 D. S. Smith, S. Fayette, S. Grandjean, C. Martin, R. Telle and T. Tonnessen, *J. Am. Ceram. Soc.*, 2003, **86**, 105–111.

139 D. Kunii and J. M. Smith, *AIChE J.*, 1960, **6**, 71–78.

140 R. Bjørk, V. Tikare, H. L. Frandsen and N. Pryds, *J. Am. Ceram. Soc.*, 2013, **96**, 103–110.

141 T.-S. Yeh and M. D. Sacks, *J. Am. Ceram. Soc.*, 1988, **71**, C484–C487.

142 C. Qian, K. Hu, Z. Shen, Q. Wang, P. Li and Z. Lu, *Ceram. Int.*, 2023, **49**, 17506–17523.

143 Z. Yang, Z. Yin, D. Wang, H. Wang, H. Song, Z. Zhao, G. Zhang, G. Qing, H. Wu and H. Jin, *Mater. Chem. Phys.*, 2020, **241**, 122453.

144 N. Kucukdogan, L. Aydin and M. Sutcu, *Thermochim. Acta*, 2018, **665**, 76–84.

145 I. H. Tavman, *Int. Commun. Heat Mass Transfer*, 1998, **25**, 723–732.

146 The Ceramic Society of Japan, *Handbook of Ceramics*, Gihodo Shuppan Co., Ltd., 2nd edn, 2002.

147 *JIS A5308: 2024 Ready-Mixed Concrete (In Japanese)*.

148 A. Gil, M. Medrano, I. Martorell, A. Lázaro, P. Dolado, B. Zalba and L. F. Cabeza, *Renewable Sustainable Energy Rev.*, 2010, **14**, 31–55.

149 S. Hasnain, *Energy Convers. Manage.*, 1998, **39**, 1127–1138.

150 T. Bauer, N. Pfleger, N. Breidenbach, M. Eck, D. Laing and S. Kaesche, *Appl. Energy*, 2013, **111**, 1114–1119.